

A single XLF dimer bridges DNA ends during nonhomologous end joining

Thomas G. W. Graham^{1,2,4}, Sean M. Carney^{2,4}, Johannes C. Walter^{2,3} and Joseph J. Loparo^{2*}

Nonhomologous end joining (NHEJ) is the primary pathway of DNA double-strand-break repair in vertebrate cells, yet how NHEJ factors assemble a synaptic complex that bridges DNA ends remains unclear. To address the role of XRCC4-like factor (XLF) in synaptic-complex assembly, we used single-molecule fluorescence imaging in *Xenopus laevis* egg extract, a system that efficiently joins DNA ends. We found that a single XLF dimer binds DNA substrates just before the formation of a ligation-competent synaptic complex between DNA ends. The interaction of both globular head domains of the XLF dimer with XRCC4 is required for efficient formation of this synaptic complex. Our results indicate that, in contrast to a model in which filaments of XLF and XRCC4 bridge DNA ends, binding of a single XLF dimer facilitates the assembly of a stoichiometrically well-defined synaptic complex.

Canonical NHEJ is the major pathway of DNA double-strand break (DSB) repair in vertebrate cells. Successful rejoining of broken DNA ends requires that they be held together in a manner that permits their processing and ligation. DNA ends are first bound by the Ku heterodimer, composed of Ku70 and Ku80, which fits over the DNA end like a ring¹. Ku recruits the DNA-dependent protein kinase catalytic subunit (DNA-PKcs), whose kinase activity is required for efficient end joining^{2–4}. Ends are ultimately ligated by DNA ligase 4 (LIG4), which resides in a complex with XRCC4 (refs^{5,6}). A homolog of XRCC4, named XLF or Cernunnos, was identified as an XRCC4-interacting protein whose disruption in humans results in immunodeficiency, developmental defects, and cellular radiosensitivity^{7,8}. Despite the identification of these core components of the NHEJ machinery, the nature of the synaptic complex that aligns broken DNA ends, in particular the roles of XLF and XRCC4–LIG4, remains poorly defined.

Structural characterization of XLF and XRCC4 has revealed that both proteins form symmetric homodimers that interact through their globular head domains^{9–14}, and mutations in XLF or XRCC4 that disrupt this interaction impair NHEJ in cell culture–based assays^{15–17}. Two possible roles of the XLF–XRCC4 interaction in NHEJ have been proposed. First, XLF may directly promote catalysis by XRCC4–LIG4. XLF stimulates XRCC4–LIG4 activity in vitro, especially on noncohesive and mismatched ends^{17–21}. XLF likewise increases the rate of LIG4 autoadenylation, the initial step in the LIG4 catalytic cycle²². The second proposal is that alternating filaments of XLF and XRCC4 bridge broken DNA ends. Filaments of purified XLF and XRCC4 are seen in crystal structures and electron micrographs^{12–14,23–25}, and a mixture of XLF and XRCC4 bridges DNA molecules in bulk and single-molecule assays^{16,17,25,26}. Additionally, super-resolution imaging of fixed cells stained with anti-XLF or anti-XRCC4 antibodies has revealed elongated nuclear foci proposed to be XLF–XRCC4 filaments²⁷. Although these results are suggestive, XLF–XRCC4 filaments have not been demonstrated to be necessary for physiological end joining.

To study the role of the XLF–XRCC4 interaction in NHEJ, we used *Xenopus laevis* egg extract, which performs efficient NHEJ

dependent on the core pathway components Ku, DNA-PKcs, XLF, XRCC4, and LIG4 (refs^{28–38}). We previously combined this cell-free system with a single-molecule Förster resonance energy transfer (smFRET) assay that allowed us to visualize synapsis of single pairs of DNA ends during NHEJ^{37,38}. These experiments revealed a step-wise transition from an initial ‘long-range’ synaptic complex (LR complex), in which DNA ends are physically tethered but not held closely together, to a ‘short-range’ synaptic complex (SR complex), in which DNA ends are closely aligned for ligation. The SR complex either ligates DNA ends or dissociates, requiring another round of SR-complex formation before eventual ligation. Formation of the LR complex requires Ku and DNA-PKcs, in agreement with the previously reported dimerization and DNA end-bridging activities of the DNA-PK holoenzyme^{39–42}. Transition from the LR complex to the SR complex requires DNA-PK catalytic activity, XLF, and XRCC4–LIG4, but not LIG4 catalytic activity. A noncatalytic role of LIG4 in the stable bridging of DNA ends is consistent with previous results from pulldown experiments in mammalian cell-free extracts⁴³. A subsequent study in a reconstituted mixture of human NHEJ proteins has indicated a transition from a transient synaptic complex dependent on Ku and DNA-PKcs to a more stable complex dependent on XLF and XRCC4–LIG4 (ref.⁴⁴). These observations closely parallel our results in *Xenopus* egg extract, thus suggesting that the mechanisms of synaptic-complex assembly are conserved between frogs and humans.

Here, we investigated the role of the XLF–XRCC4 interaction in synaptic-complex formation. Using *X. laevis* egg extract, we show that the XLF–XRCC4 interaction is required for formation of the SR complex. In three-color single-molecule imaging experiments, we visualized binding of fluorescently labeled XLF protein to individual DNA substrates undergoing synapsis. Strikingly, formation of the SR complex involves association of only a single XLF dimer with DNA ends. Experiments with a synthetic XLF tandem dimer imply that XLF nonetheless interacts with XRCC4 through both globular head domains of the XLF dimer. These results support a model in which XLF binds with defined stoichiometry to the synaptic complex, thereby facilitating a structural rearrangement that closely aligns DNA ends.

¹Department of Systems Biology, Harvard Medical School, Boston, MA, USA. ²Department of Biological Chemistry and Molecular Pharmacology, Harvard Medical School, Boston, MA, USA. ³Howard Hughes Medical Institute, Harvard Medical School, Boston, MA, USA. ⁴These authors contributed equally: Thomas G. W. Graham, Sean M. Carney. *e-mail: joseph_loparo@hms.harvard.edu

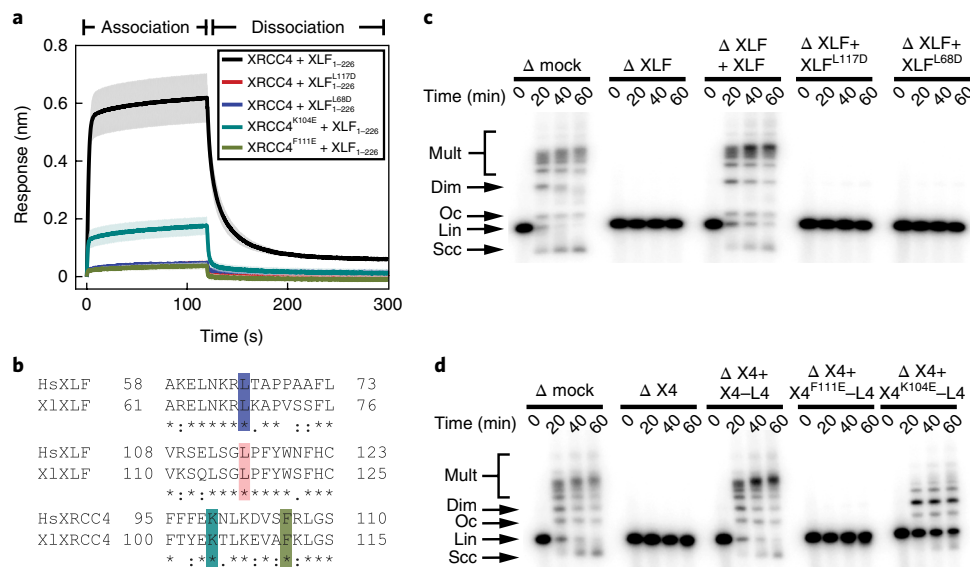


Fig. 1 | XLF-XRCC4 interaction is required for NHEJ in *Xenopus* egg extract. **a**, BLI measurements of interaction between point mutants of XRCC4 and C-terminally truncated XLF (XLF¹⁻²²⁶). Traces represent the average, and the shading around each trace represents the s.d. of three replicates. **b**, Alignment of human (Hs) and *Xenopus laevis* (XI) XLF and XRCC4 around residues required for the XLF-XRCC4 interaction: XILF L68 (HsXLF L65, blue)¹³, XILF L117 (HsXLF L115, red)¹³, XIXRCC4 K104 (HsXRCC4 K99, cyan)^{11,16}, and XIXRCC4 F111 (HsXRCC4 F106, chartreuse)¹³. **c,d**, Bulk NHEJ assay in egg extract immunodepleted of XLF (**c**) or XRCC4 (**d**) and supplemented with purified recombinant protein. The molar ratio of recombinant protein-DNA ends for XLF and XRCC4-LIG4 in the rescue experiments shown in **c** and **d** is 500:1 and 50:1, respectively. Δ mock, immunodepletion with nonspecific rabbit IgG; ΔX4, XRCC4 depletion, ΔXLF, XLF depletion; X4-L4, recombinant XRCC4-LIG4 complex. DNA species: scc, supercoiled closed circular; lin, linear; oc, open circular; dim, dimer; mult, multimer. Uncropped images of **c** and **d** are shown in Supplementary Dataset 1.

Results

XLF-XRCC4 interaction is required for end joining in *Xenopus* egg extract. To explore the function of the XLF-XRCC4 interaction during physiological end joining, we first tested whether *Xenopus laevis* XLF and XRCC4 interact. To this end, we used biolayer interferometry (BLI) to measure the association of *X. laevis* XLF with immobilized *X. laevis* XRCC4 (unless otherwise specified, XLF and XRCC4 refer to the *X. laevis* proteins herein). Full-length XLF bound XRCC4 and only partially dissociated when washed with buffer, thus suggesting irreversible aggregation on the surface (Supplementary Fig. 1a). Similar aggregation was previously observed in surface plasmon resonance experiments with human XLF and XRCC4 (ref. ¹⁰). However, a truncated version of XLF lacking the unstructured C-terminal region (XLF¹⁻²²⁶, corresponding to human XLF¹⁻²²⁴ (ref. ¹³)) bound XRCC4 and completely dissociated when washed with buffer (Fig. 1a and Supplementary Fig. 1b). *X. laevis* XLF¹⁻²²⁶ and XRCC4 interacted with slightly higher affinity than previously reported for the human XLF and XRCC4 (apparent K_d of $0.28 \pm 0.03 \mu\text{M}$, compared with $1.2 \mu\text{M}$ to $7.8 \mu\text{M}$ for human (h) hXLF-hXRCC4; cf. BLI of XRCC4 binding below and Supplementary Table 1)^{10,13,45}. Thus, XLF-XRCC4 interaction is conserved between *Xenopus* and humans. Dynamic light scattering (DLS) revealed that XRCC4 and XLF formed large complexes when mixed, thus suggesting assembly of filaments (Supplementary Fig. 1c). In addition, similarly to human XLF and XRCC4, a mixture of XLF and XRCC4, but neither protein alone, bridged DNA in pull-down experiments (Supplementary Fig. 1d). Thus, XLF-XRCC4 interaction, in vitro filament formation, and DNA bridging are conserved between *X. laevis* and humans.

Mutations of human XLF and XRCC4 that disrupt the interaction between the two proteins have been found to impair NHEJ in cell-based assays^{13,15-17}. We tested the effect of generating the corresponding mutations in the *X. laevis* proteins (Fig. 1b). Interaction between XLF and XRCC4 was abolished by the XLF L68D and L117D mutations and by the XRCC4 F111E mutation (Fig. 1a,b).

The XRCC4 K104E mutation weakened but did not eliminate interaction with XLF (Fig. 1a), thus reflecting a higher dissociation rate (Supplementary Fig. 1e,f). The denaturation temperatures of all mutants, measured by differential scanning fluorimetry, were within 1.45°C of the wild-type (WT) protein, thus suggesting that the defect is not due to large-scale misfolding (Supplementary Fig. 1g). Mutations that disrupted the XLF-XRCC4 interaction also disrupted formation of large XLF-XRCC4 complexes in DLS experiments and abolished DNA bridging in pulldown experiments (Supplementary Fig. 1c,d).

We next tested whether interaction-deficient XLF and XRCC4 mutants might support cell-free NHEJ. Egg extract was immunodepleted of XLF or XRCC4, thus abolishing end joining of linear DNA substrates (Fig. 1c,d and ref. ³⁸). This effect was fully rescued by addition of recombinant XLF to XLF-depleted extract (Fig. 1c) or by addition of recombinant XRCC4-LIG4 to XRCC4-depleted extract (Fig. 1d; of note, depletion of XRCC4 codepletes LIG4 (ref. ³⁸)). In contrast, XLF^{L117D} and XLF^{L68D} did not rescue end joining in XLF-depleted egg extract (Fig. 1c), and XRCC4^{F111E}-LIG4 did not rescue end joining in XRCC4-depleted extract (Fig. 1d). XRCC4^{K104E}-LIG4 partially rescued end joining in XRCC4-depleted extract (Fig. 1d), in agreement with the residual low-affinity interaction between XRCC4^{K104E} and XLF (Fig. 1a and Supplementary Fig. 1e,f). Together, these results suggest that in frog egg extract, as in mammals, the interaction between XLF and XRCC4 is required for end joining.

XLF-XRCC4 interaction is required for short-range synopsis of DNA ends. We previously described two related single-molecule fluorescence assays for monitoring synaptic-complex formation in egg extract³⁸. In the ‘intermolecular’ assay, a surface-tethered DNA duplex labeled with Cy3 is exposed to extract containing a DNA duplex labeled with Cy5. Colocalization of Cy3 and Cy5 without FRET reports on the formation of the LR complex, whereas the appearance of FRET indicates the formation of the SR complex,

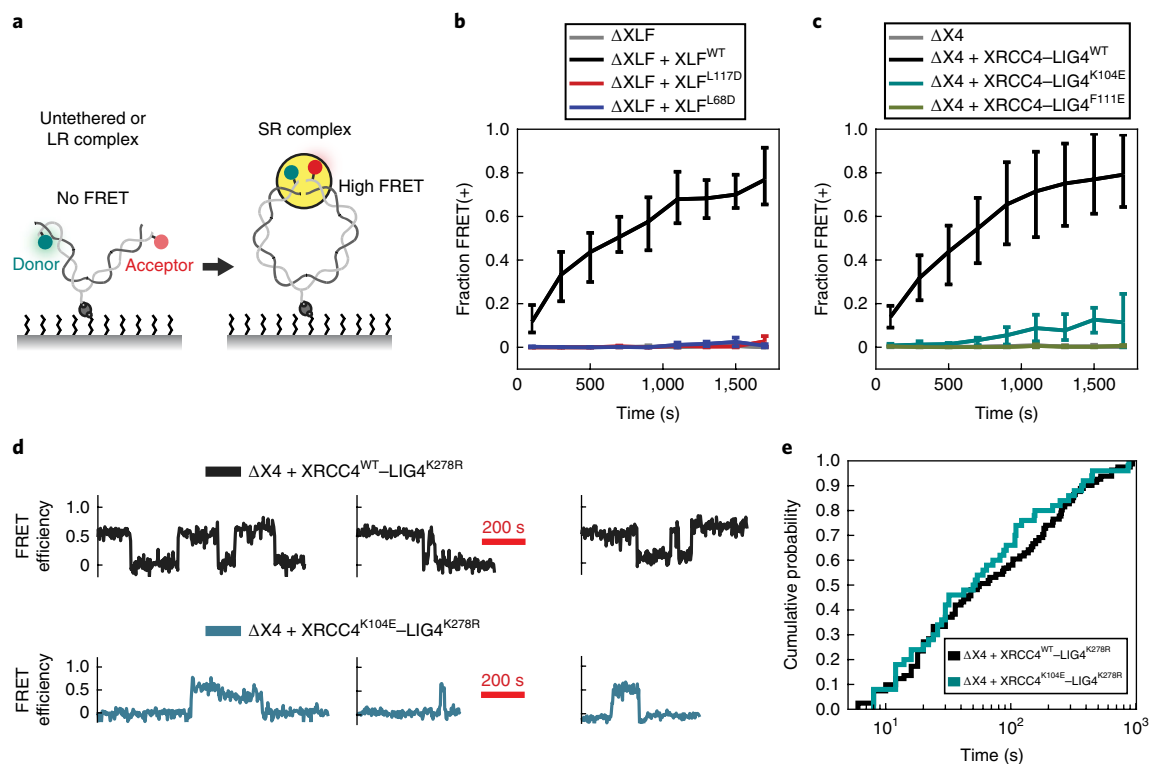


Fig. 2 | XLF-XRCC4 interaction is required for SR-complex formation. **a**, Schematic of intramolecular smFRET reporter for monitoring SR-complex formation³⁸. DNA is tethered internally via a biotin-streptavidin interaction and labeled 7 bp from each end with Cy3 (donor) and Cy5 (acceptor) fluorophores. No FRET is detected when DNA ends are untethered or in the LR complex. Close alignment of DNA ends within the SR complex is indicated by energy transfer between Cy3 and Cy5. **b,c**, Kinetics of SR-complex formation in extract depleted of XLF or XRCC4 and supplemented with purified recombinant protein, as in Fig. 1c,d. The mean fraction of FRET-positive (SR complex or ligated) substrates is plotted as a function of time after extract addition. Bars indicate the minimum and maximum values obtained from multiple experimental replicates (n values in Supplementary Table 2). Source data for **b** and **c** are available with the paper online. **d**, Sample smFRET trajectories showing SR-complex formation and dissociation in XRCC4-immunodepleted extract supplemented with either XRCC4^{WT}-LIG4^{K278R} or XRCC4^{K104E}-LIG4^{K278R}. Catalytically inactive LIG4^{K278R} was used here and in **e** to prevent ligation of DNA ends. **e**, Cumulative distribution functions of SR-complex lifetimes. The difference between the two conditions was not statistically significant ($P=0.45$, log-rank test; sample sizes in Supplementary Table 3). The data shown in **b** and **c** were collected with a 0.5-s exposure time, alternating between two frames of Cy3 excitation and one frame of Cy5 excitation. The data shown in **d** and **e** were collected with a 1-s exposure with a 1-s delay between exposures, alternating between four frames of Cy3 excitation and one frame of Cy5 excitation.

in which DNA ends are closely aligned and poised for ligation. To increase the efficiency of SR-complex formation, we also used an intramolecular assay in which a 2-kb DNA substrate labeled 7 nt from one end with Cy3 and 7 nt from the other end with Cy5 is tethered to a glass coverslip via an internal biotin (Fig. 2a). FRET between Cy3 and Cy5, detected by TIRF microscopy, indicates assembly of the SR complex. Because the Cy3 and Cy5 labels on the intramolecular substrate always colocalize, this assay cannot detect LR-complex assembly.

Given our previous demonstration that XLF and XRCC4-LIG4 are dispensable for LR-complex formation³⁸, we used the intramolecular assay to address whether the XLF-XRCC4 interaction is required for SR-complex formation. For these experiments, many fields of view were imaged sequentially, and the fraction of DNA substrates with FRET efficiency > 0.25 was plotted as a function of time after extract addition (Fig. 2b,c). As shown previously³⁸, depletion of XLF or XRCC4 abolished SR-complex formation, and these defects were rescued by purified recombinant XLF or XRCC4-LIG4, respectively (Fig. 2b,c). In contrast, interaction-deficient XLF^{L68D}, XLF^{L117D}, and XRCC4^{F111E}-LIG4 did not support SR-complex formation (Fig. 2b,c), whereas XRCC4^{K104E}-LIG4 exhibited low activity, in agreement with its residual binding to XLF (Fig. 2c). Thus, a physical interaction between XLF and XRCC4 is required for the close alignment of DNA ends within the SR synaptic complex.

The above results do not distinguish whether XLF-XRCC4 interaction is required for the formation or maintenance of the SR complex. To address this question, we performed long time-course imaging experiments to compare the kinetics of SR-complex formation and dissociation in the presence of WT XRCC4 and the hypomorphic K104E mutant. To prevent ligation of DNA substrates in these experiments, we supplemented extract immunodepleted of XRCC4 with XRCC4 WT or K104E in complex with catalytically inactive LIG4^{K278R}. The SR complex formed at a fivefold-slower rate in the presence of XRCC4^{K104E} compared with XRCC4^{WT} ($2.7 \times 10^{-4} \pm 0.5 \times 10^{-4} \text{ s}^{-1}$, s.e.m., compared with $1.4 \times 10^{-3} \pm 0.3 \times 10^{-3} \text{ s}^{-1}$, s.e.m.), thus suggesting that the XLF-XRCC4 interaction is required for efficient establishment of the SR complex. Once formed, however, the SR complex had an equivalent lifetime in the presence of XRCC4^{K104E} ($129 \pm 27 \text{ s}$) and XRCC4^{WT} ($153 \pm 23 \text{ s}$) (Fig. 2d,e), thus suggesting that the stability of the assembled SR complex becomes independent of XRCC4-XLF interaction. In both cases, the lifetime distribution of the SR complex is significantly nonexponential ($P < 0.001$, Lilliefors test⁴⁶), thus indicating that SR-complex dissociation is not governed by a single rate constant.

The SR synaptic complex contains a single XLF dimer. A model in which end synapsis involves the formation of XLF-XRCC4

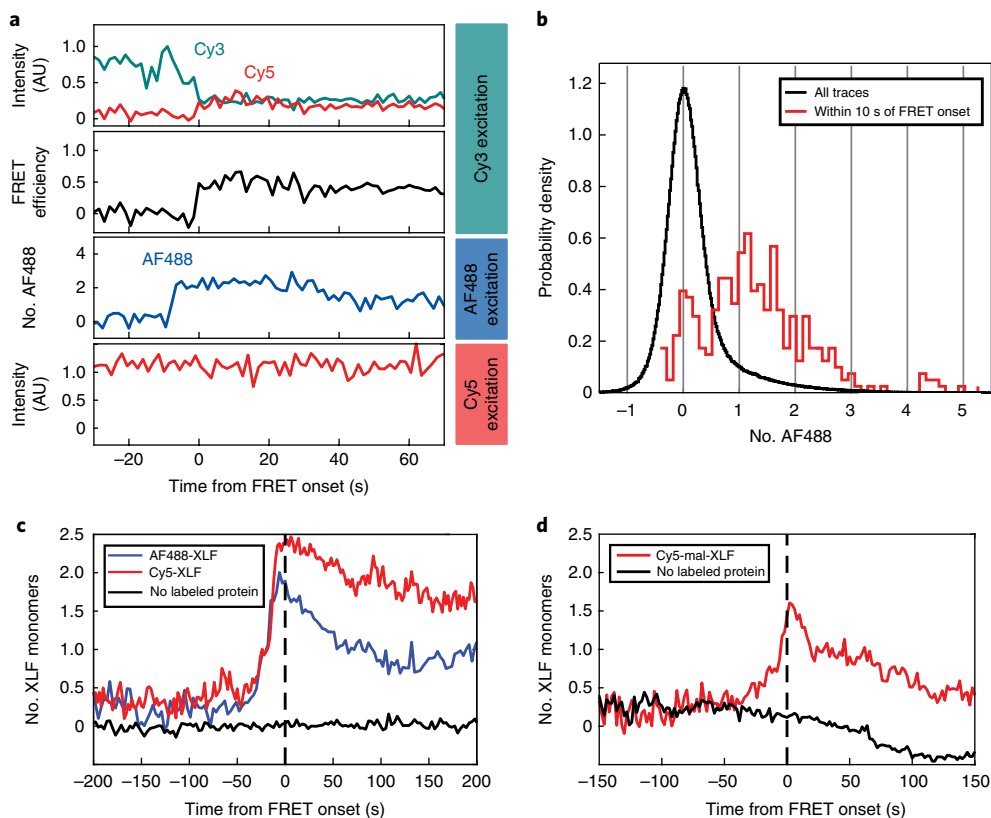


Fig. 3 | Three-color imaging of XLF binding and SR-complex formation. **a**, Three-color single-molecule imaging of FRET between Cy3 and Cy5-labeled DNA ends, along with binding of Halo-tagged XLF protein labeled with Alexa Fluor 488 (AF488-XLF). Top panel, intensity in the Cy3 (cyan) and Cy5 (red) channels with excitation of Cy3. Second panel, calculated Cy3-Cy5 FRET efficiency. Third panel, AF488 intensity, expressed as a multiple of the average intensity of single-AF488 reference spots. Bottom panel, Cy5 intensity with direct excitation. Additional traces in Supplementary Fig. 2f. AU, arbitrary units. **b**, Histogram of AF488 intensity, expressed as a multiple of the average intensity of single-AF488 reference spots. The black curve includes all substrates, and the red curve includes only the subset of frames within 10 s of the transition to high FRET. **c**, Average of AF488-XLF and Cy5-XLF stoichiometry for traces aligned at the time of FRET onset. AF488 intensity, normalized to the intensity of single-AF488 reference spots, was divided by the protein labeling fraction to give XLF protein stoichiometry. Cy5 intensity, normalized to single-Cy5 intensity (Supplementary Fig. 3a), was divided by the protein-labeled fraction after subtracting 1 to account for the single Cy5 label on the DNA. Black curve shows data from a mock AF488 imaging experiment without AF488-XLF protein. **d**, Average stoichiometry of XLF nonspecifically labeled on cysteines with Cy5-maleimide, aligned at the time of FRET onset. Cy5-mal-XLF stoichiometry was calculated as for Cy5-XLF in **c**. Black curve shows data from a control experiment in the absence of Cy5-mal-XLF. The decay of the black curve below zero results from photobleaching of the Cy5 label on DNA.

filaments predicts binding of numerous XLF dimers to each pair of DNA ends. To determine the stoichiometry of XLF within the synaptic complex, we used three-color imaging of Cy3/Cy5-labeled DNA ends and Alexa Fluor 488-labeled, Halo-tagged XLF (AF488-XLF). AF488-XLF rescued end joining in XLF-immunodepleted extract, thus demonstrating that XLF labeled in this manner is functional (Supplementary Fig. 2a). Three-color imaging allowed us to quantify binding of AF488-XLF to DNA substrates while also monitoring FRET between Cy3- and Cy5-labeled DNA ends (Fig. 3a). Biotinylated AF488-Halo tag deposited on the coverslip surface was used as an internal standard to determine the intensity of single AF488 fluorophores in egg extract (Methods).

At any instant, most DNA substrates exhibited no AF488 signal (Fig. 3b, black curve). Given that AF488-XLF monomer was 68% labeled, on the basis of UV-visible absorbance measurements (Methods), this result implies low average occupancy of XLF on DNA substrates, and it is inconsistent with widespread formation of XLF-XRCC4 filaments under these conditions. We next focused on substrates that undergo a transition to the SR complex, as indicated by the appearance of FRET between Cy3 and Cy5. Strikingly, SR-complex formation was typically preceded by step-like AF488-XLF binding events (Fig. 3a and Supplementary Fig. 2f).

The number of AF488 fluorophores present within 10 s of SR-complex formation, determined by comparison with the internal single-AF488 standard, was mostly between 0 and 2 (Fig. 3b, red curve), in agreement with binding of a single incompletely labeled dimer of XLF. To test this interpretation, we fit the distribution of fluorophore number in the AF488 frame just before SR-complex formation to a binomial distribution with $n=2$ (Supplementary Fig. 2e). The fraction of labeled XLF obtained from the fit (0.60; bootstrap 95% confidence interval, 0.46–0.71) is in good agreement with the value of 0.68 estimated from absorbance measurements. An ensemble average of XLF stoichiometry, aligned at the time of SR-complex formation and corrected for the labeled fraction, showed a peak occupancy of approximately two XLF monomers (i.e., one XLF dimer) several seconds before SR-complex formation (Fig. 3c, blue curve). No such peak was observed in the absence of labeled protein (Fig. 3c, black curve), thus ruling out a photophysical artifact. Similar results were obtained when Halo-XLF was labeled with Cy5 (Cy5-XLF; Fig. 3c, red curve, and Supplementary Fig. 3a–c). Remarkably, despite the ability of Halo-XLF to support NHEJ with similar efficiency as untagged XLF (Supplementary Fig. 2a), a mixture of Halo-XLF and XRCC4 did not bridge DNA in bulk pull-down experiments (Supplementary Fig. 1h), thus indicating that the

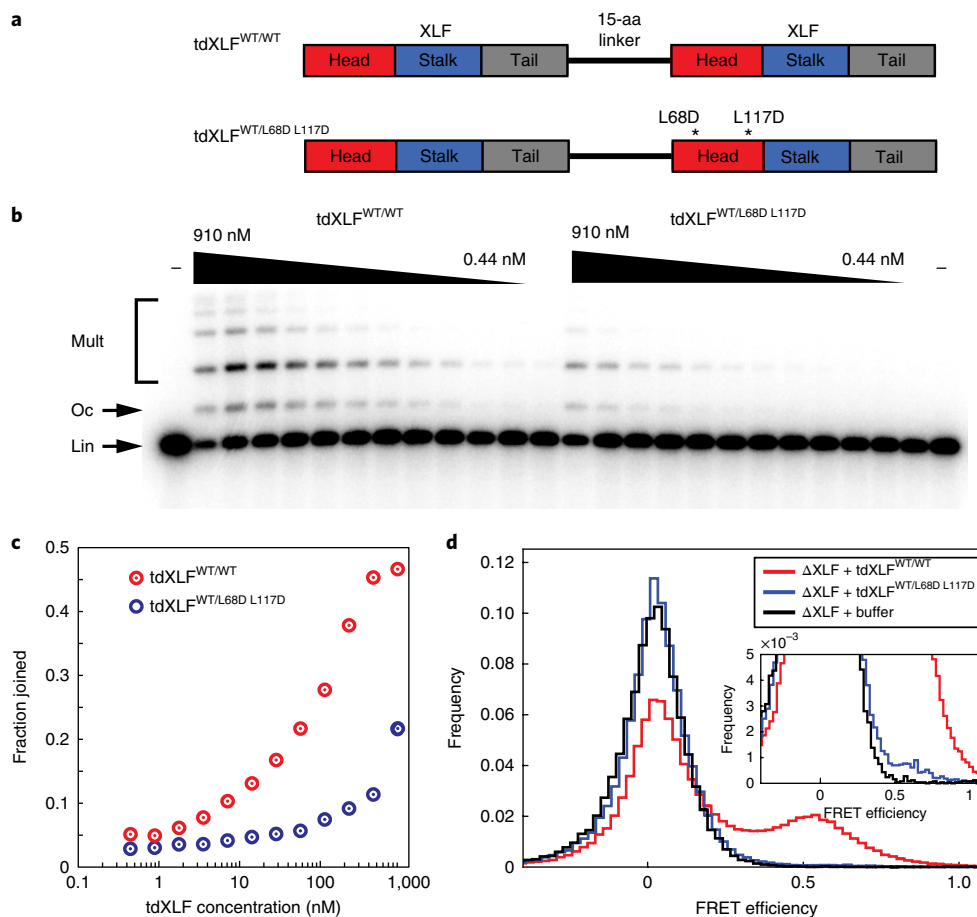


Fig. 4 | End joining in the presence of a synthetic tandem dimer of XLF. **a**, Schematic of the XLF tandem dimer (tdXLF) construct. Two XLF coding sequences are concatenated by a flexible 15-aa linker. Asterisks denote point mutations. **b**, Dose dependence of end joining as a function of tdXLF concentration for WT/WT and WT/L68D L117D constructs. Black wedges represent a twofold serial dilution series from 910 nM to 0.44 nM. Control reactions not supplemented with tdXLF are labeled '-'. Lin, linear DNA substrate; oc, open-circular product; mult, dimeric and multimeric products. Uncropped image in Supplementary Dataset 1. **c**, Quantification of product formation in the gel in **b**. Fraction joined was quantified as background-subtracted intensity of product bands divided by total background-subtracted intensity of substrate and product bands. Source data for **c** are available online. **d**, Histogram of FRET efficiency from tdXLF rescue of smFRET intramolecular circularization experiments, accumulated over 20 min.

DNA-bridging activity detected by this pulldown assay is not essential for NHEJ. To ensure that the observed low stoichiometry of XLF in single-molecule experiments was not due to the inability of Halo-XLF to form DNA-bridging filaments with XRCC4, we labeled untagged XLF on endogenous cysteines with Cy5-maleimide. Cy5-maleimide-labeled XLF (Cy5-mal-XLF) rescued end joining in XLF-depleted extract (Supplementary Fig. 3d), and, unlike Halo-XLF, it assembled DNA-bridging complexes with XRCC4 in bulk pulldown experiments (Supplementary Fig. 3e). Nonetheless, Cy5-mal-XLF still bound with an average stoichiometry consistent with one dimer per DNA substrate at the time of SR-complex formation (Fig. 3d). These results suggest that SR-complex formation involves binding of a single XLF dimer.

End synopsis requires interaction of both XLF head domains with XRCC4. Although our data indicate that extensive XLF–XRCC4 filaments are not required for SR-complex formation, the possibility remained that both subunits of the XLF dimer might be required to interact with XRCC4. To address this possibility, we generated an XLF tandem dimer construct (tdXLF; Fig. 4a) in which the number of XRCC4 interaction sites could be precisely defined. tdXLF had the same molecular weight as the WT XLF dimer, as measured by size-exclusion chromatography with multiangle light scattering (Supplementary Fig. 4a,b). End joining in XLF-immunodepleted

egg extract was rescued by tdXLF, thus demonstrating that this construct functioned in NHEJ (Fig. 4b,c).

To test whether interaction with XRCC4 on both sides of the XLF dimer is required for end joining, we supplemented XLF-depleted extract with tdXLF^{WT/WT} or tdXLF^{WT/L68D L117D}, in which the second XLF sequence in the tandem dimer was mutated to prevent interaction with XRCC4 (Fig. 4a). Whereas tdXLF^{WT/L68D L117D} partially rescued end joining, its activity was impaired ~8- to 16-fold relative to tdXLF^{WT/WT}—an impairment greater than would be expected from a 50% decrease in the effective concentration of WT XLF head domains (Fig. 4b,c). Equivalent results were obtained for the tdXLF^{WT/L117D} single mutant (data not shown). Importantly, tdXLF^{WT/L68D L117D} exhibited a 15-fold decrease in the SR-complex formation rate ($1.9 \times 10^{-4} \pm 1.1 \times 10^{-4} \text{ s}^{-1}$) relative to tdXLF^{WT/WT} ($2.8 \times 10^{-3} \pm 1.1 \times 10^{-3} \text{ s}^{-1}$) in intramolecular smFRET circularization assays (Fig. 4d). However, a low level of SR-complex formation and end joining still occurred (Fig. 4b–d). Given the presence of two interaction-blocking mutations, this residual activity of tdXLF^{WT/L68D L117D} is unlikely to reflect binding of the mutant head domain to XRCC4. Thus, binding of XRCC4 to both head domains of XLF is required to form the SR complex with normal efficiency, whereas binding of a single XLF head domain to XRCC4 permits SR-complex formation at a substantially slower rate.

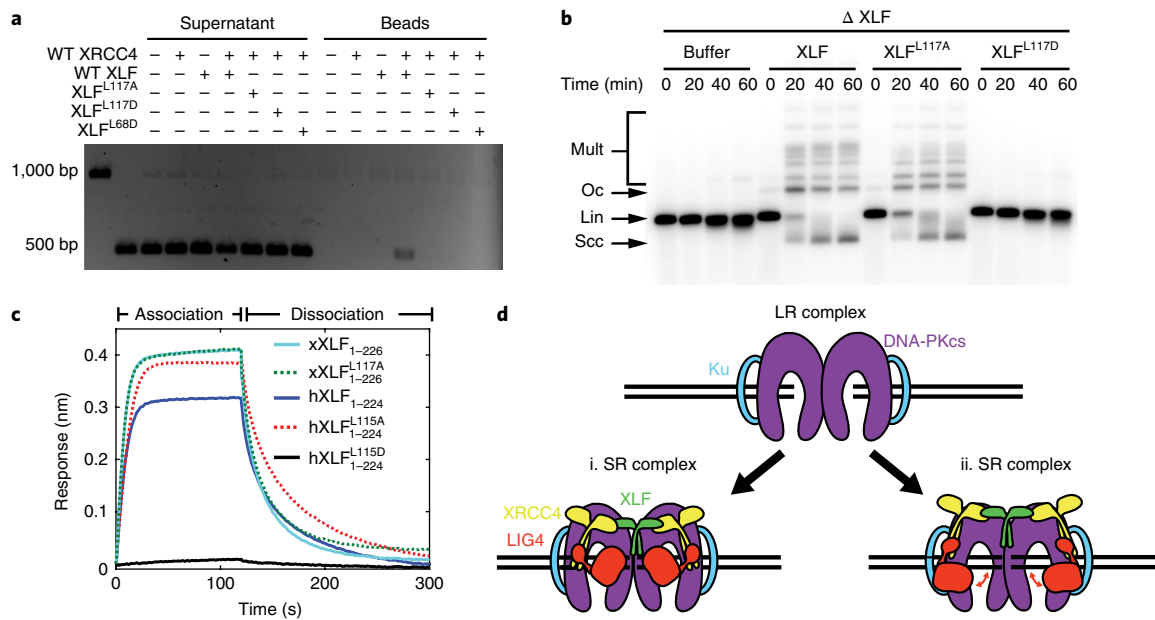


Fig. 5 | Characterization of human XLF^{L115A} and *Xenopus* XLF^{L117A}. **a**, XLF–XRCC4 DNA pull-down assay. Beads coated with a biotinylated 1,000-bp DNA fragment were incubated with a soluble 500-bp DNA fragment and the indicated proteins. Deproteinized supernatant and bead-bound fractions were separated on a 1× Tris–borate–EDTA agarose gel. 1,000- and 500-bp DNA fragments alone were loaded in the first two lanes. **b**, Bulk NHEJ assay in egg extract immunodepleted of XLF (Δ XLF) and supplemented with purified recombinant protein. Lin, linear substrate; oc, open-circular products; sc, supercoiled closed-circular products; mult, dimeric and higher-order multimeric products. Uncropped images of **a** and **b** are shown in Supplementary Dataset 1. **c**, BLI of XRCC4 binding by WT and L115A or L117A mutant human and *Xenopus* XLF. Response curves represent the average of two experimental replicates for each condition. XLF variants were tested at a concentration of 250 nM, with the exception of hXLF^{L115D} 1–224, which was tested at 2 μ M. Fitted K_{on} and K_{off} values are listed in Supplementary Table 1. Source data for **c** are available online. **d**, Model of the role of XLF in SR-complex assembly. Binding of both head domains of XLF to XRCC4–LIG4 is required for SR-complex formation, which may involve (i) direct engagement of both DNA ends by the XLF–XRCC4–LIG4 ternary complex or (ii) a conformational change in the DNA–PK holoenzyme that is facilitated allosterically by binding of the XLF–XRCC4–LIG4 ternary complex. In the latter model, conformational flexibility in LIG4 (red double arrows) permits binding and unbinding of the LIG4 catalytic domain to DNA ends.

As an independent means of examining the requirement for XRCC4–XLF interaction through both XLF head domains, we generated synthetic XLF heterodimers by coexpression of XLF monomers with different affinity tags, then performed tandem affinity purification (Methods). The exchange of monomers between purified XLF dimers was negligible (Supplementary Fig. 4c,d). In agreement with results for tdXLF, XLF heterodimers with one WT subunit and one L117D mutant subunit were severely deficient in end joining, as compared with WT–WT heterodimers (Supplementary Fig. 4e,f). Together, these results indicate that efficient SR-complex formation and end joining require that both head domains of a single XLF monomer interact with XRCC4.

NHEJ requires XLF–XRCC4 binding but not DNA bridging by filaments. As noted above, N-terminally Halo-tagged XLF supports end joining despite being unable to bridge DNA in a pull-down assay (Supplementary Figs. 1h and 2a). The behavior of this fusion protein is reminiscent of that of the L115A mutant of human XLF, which cannot bridge DNA in vitro yet rescues the DNA-damage sensitivity of various XLF-deficient cell lines^{17,47}. To investigate further whether the in vitro DNA-bridging activity of XLF is separable from its function in end joining, we examined the corresponding L117A mutant in *X. laevis* XLF. Similarly to hXLF^{L115A}, XLF^{L117A} did not bridge DNA in pull-down experiments with XRCC4 (Fig. 5a). However, XLF^{L117A} supported robust end joining in XLF-immunodepleted egg extract (Fig. 5b). Previous results from a native-PAGE binding assay suggest that hXLF^{L115A} is deficient in interacting with XRCC4 (ref. 11). In contrast, our quantitative BLI measurements revealed that both hXLF^{L115A} and *Xenopus* XLF^{L117A}

interact with XRCC4 with apparent K_d values similar to those of WT XLF (Fig. 5c and Supplementary Table 1). The finding that XLF^{L117A} (hXLF^{L115A}) interacts with XRCC4 and supports NHEJ despite not bridging DNA in vitro suggests that DNA bridging by XLF–XRCC4 filaments is not essential for NHEJ.

Discussion

Despite years of study, the mechanism of DNA-end synapsis during NHEJ has remained elusive. To address this problem, we used *Xenopus* egg extract, which contains the entire soluble egg proteome and supports highly efficient end joining that requires all four core NHEJ factors (Ku, DNA–PKcs, XLF, and XRCC4–LIG4). Using single-molecule imaging in egg extract, we found that the XLF–XRCC4 interaction is essential for close alignment of DNA ends within the SR complex. We further demonstrated that a single XLF dimer, interacting with XRCC4 through both head domains, binds DNA ends immediately before SR-complex formation. Our results shed light on the previously obscure role of XLF in NHEJ and indicate that end joining involves the juxtaposition of DNA ends in a stoichiometrically well-defined complex.

Our results suggest that within the SR complex, a single XLF dimer bridges two XRCC4–LIG4 complexes (Fig. 5d). Formation of an (XLF)₂–((XRCC4)₂–LIG4)₂ ternary complex is consistent with results from size-exclusion chromatography of XLF–XRCC4–LIG4 mixtures⁴⁸. Such a complex has also been proposed on the basis of structural data suggesting that steric occlusion from full-length LIG4 may permit binding of only a single XLF dimer to XRCC4–LIG4 (refs 13,15). Precisely how the XLF–XRCC4–LIG4 ternary complex facilitates SR-complex formation remains unclear.

One possibility is that DNA-binding motifs from XLF, XRCC4, and LIG4 directly contact DNA ends and bring them together (Fig. 5d, i). Alternatively, assembly of the XLF–XRCC4–LIG4 sub-complex within the DNA-PK holoenzyme may induce a conformational transition of DNA-PK that aligns DNA ends (Fig. 5d, ii). In support of the latter model, the SR complex remains stable in the presence of XRCC4^{K104E}, which dissociates much more rapidly from XLF than does WT XRCC4, thus suggesting that XLF–XRCC4 interactions are required only for the initial formation of the SR complex but not for its maintenance (Fig. 2e). Given that the lifetime of the SR complex is nonexponentially distributed, characterizing the multiple kinetic steps involved in SR-complex dissociation and determining which factors influence these steps should be interesting.

There are several conceptual problems associated with the XLF–XRCC4 filament model. First, end-bridging filaments of XLF–XRCC4 should block LIG4 and other end-processing enzymes from gaining access to the DNA ends⁴⁹. Second, how the inner channel of these filaments could accommodate the large size of DNA-PKcs is unclear. Third, some mechanism would be needed to promote stable assembly of filaments near DNA ends while preventing their assembly on the much larger quantity of unbroken DNA in the cell. Fourth, phosphorylation of XLF and XRCC4 by DNA-PK inhibits filament formation, an effect that would be expected to suppress rather than promote filament assembly near DNA ends^{16,45}. In contrast, none of these difficulties apply to a model in which XLF and XRCC4 form a short oligomer within a stoichiometrically defined synaptic complex.

Our experiments cannot rule out the possibility that XLF and XRCC4 might form filaments in cells. For instance, other protein–protein interactions might concentrate XLF and XRCC4 within chromosomal DNA-damage-response foci in a manner that is not recapitulated on the relatively short DNA substrates in our assay. However, our observation of efficient NHEJ in the absence of XLF–XRCC4 filaments shows that these structures are not required and suggests that a careful reappraisal of the filament model is needed. In vitro DNA-bridging experiments with purified XLF and XRCC4 have generally used buffers with low ionic strength (25–75 mM KCl). In contrast, we found that DNA pulldown by XLF–XRCC4 mixtures, as well as formation of large complexes measured by dynamic light scattering, was abolished at a more physiological salt concentration of 150 mM (Supplementary Fig. 1h,i). A more direct line of evidence supporting XLF–XRCC4 filament formation in cells has come from super-resolution imaging of fixed cells stained with antibodies against XLF and XRCC4 (ref. 27). XLF and XRCC4 appeared punctate in these experiments, and a subset of puncta exhibited an elongated morphology suggestive of filaments. However, further characterization of these structures is needed, because colocalization of points in super-resolution imaging does not prove the existence of physically continuous filaments. Moreover, whether XLF–XRCC4 interaction is required for focus formation remains to be tested (e.g., by analysis of mutants).

Previously, human XLF^{L115A} was shown to rescue the DNA-damage sensitivity of most XLF-deficient mammalian cell lines despite being unable to bridge DNA in vitro, thus calling into question whether XLF–XRCC4 filaments are generally required for NHEJ^{17,47}. Likewise, we observed that *X. laevis* XLF^{L117A} (corresponding to hXLF^{L115A}) and N-terminally Halo-tagged XLF supported NHEJ in egg extract despite exhibiting no DNA-bridging activity in a pulldown assay (Figs. 3a–c and 5a,b and Supplementary Figs. 1h and 2a). We found that, contrary to previous qualitative observations¹¹, hXLF^{L115A} is not deficient in hXRCC4 binding (Fig. 5c and Supplementary Table 1). These results support the idea that, as in our cell-free extract, end joining in cells requires XLF–XRCC4 interaction but not DNA bridging by XLF–XRCC4 filaments.

In summary, a single XLF dimer, interacting through both head domains with XRCC4, promotes the close alignment of DNA ends.

This result suggests that rather than being tethered by protein filaments, DNA ends are precisely aligned within a stoichiometrically defined protein complex. Reconstitution and structural characterization of this complex should be an important direction for future work.

Online content

Any methods, additional references, Nature Research Reporting Summary, source data, statements of data availability and associated accession codes are available at <https://doi.org/10.1038/s41594-018-0120-y>.

Received: 7 March 2018; Accepted: 5 July 2018;

Published online: 03 September 2018

References

- Walker, J. R., Corpina, R. A. & Goldberg, J. Structure of the Ku heterodimer bound to DNA and its implications for double-strand break repair. *Nature* **412**, 607–614 (2001).
- Dobbs, T. A., Tainer, J. A. & Lees-Miller, S. P. A structural model for regulation of NHEJ by DNA-PKcs autophosphorylation. *DNA Repair (Amst.)* **9**, 1307–1314 (2010).
- Jette, N. & Lees-Miller, S. P. The DNA-dependent protein kinase: a multifunctional protein kinase with roles in DNA double strand break repair and mitosis. *Prog. Biophys. Mol. Biol.* **117**, 194–205 (2015).
- Jiang, W. et al. Differential phosphorylation of DNA-PKcs regulates the interplay between end-processing and end-ligation during nonhomologous end-joining. *Mol. Cell.* **58**, 172–185 (2015).
- Critchlow, S. E., Bowater, R. P. & Jackson, S. P. Mammalian DNA double-strand break repair protein XRCC4 interacts with DNA ligase IV. *Curr. Biol.* **7**, 588–598 (1997).
- Grawunder, U. et al. Activity of DNA ligase IV stimulated by complex formation with XRCC4 protein in mammalian cells. *Nature* **388**, 492–495 (1997).
- Buck, D. et al. Cernunnos, a novel nonhomologous end-joining factor, is mutated in human immunodeficiency with microcephaly. *Cell* **124**, 287–299 (2006).
- Ahnesorg, P., Smith, P. & Jackson, S. P. XLF interacts with the XRCC4–DNA ligase IV complex to promote DNA nonhomologous end-joining. *Cell* **124**, 301–313 (2006).
- Junop, M. S. et al. Crystal structure of the Xrcc4 DNA repair protein and implications for end joining. *EMBO J.* **19**, 5962–5970 (2000).
- Li, Y. et al. Crystal structure of human XLF/Cernunnos reveals unexpected differences from XRCC4 with implications for NHEJ. *EMBO J.* **27**, 290–300 (2008).
- Andres, S. N., Modesti, M., Tsai, C. J., Chu, G. & Junop, M. S. Crystal structure of human XLF: a twist in nonhomologous DNA end-joining. *Mol. Cell* **28**, 1093–1101 (2007).
- Hammel, M., Yu, Y., Fang, S., Lees-Miller, S. P. & Tainer, J. A. XLF regulates filament architecture of the XRCC4–ligase IV complex. *Structure* **18**, 1431–1442 (2010).
- Ropars, V. et al. Structural characterization of filaments formed by human Xrcc4–Cernunnos/XLF complex involved in nonhomologous DNA end-joining. *Proc. Natl Acad. Sci. USA* **108**, 12663–12668 (2011).
- Hammel, M. et al. XRCC4 protein interactions with XRCC4-like factor (XLF) create an extended grooved scaffold for DNA ligation and double strand break repair. *J. Biol. Chem.* **286**, 32638–32650 (2011).
- Malivert, L. et al. Delineation of the Xrcc4-interacting region in the globular head domain of cernunnos/XLF. *J. Biol. Chem.* **285**, 26475–26483 (2010).
- Roy, S. et al. XRCC4's interaction with XLF is required for coding (but not signal) end joining. *Nucleic Acids Res.* **40**, 1684–1694 (2012).
- Roy, S. et al. XRCC4/XLF interaction is variably required for DNA repair, and is not required for Ligase IV stimulation. *Mol. Cell. Biol.* **35**, 3017–3028 (2015).
- Lu, H., Pannicke, U., Schwarz, K. & Lieber, M. R. Length-dependent binding of human XLF to DNA and stimulation of XRCC4–DNA ligase IV activity. *J. Biol. Chem.* **282**, 11155–11162 (2007).
- Gu, J., Lu, H., Tsai, A. G., Schwarz, K. & Lieber, M. R. Single-stranded DNA ligation and XLF-stimulated incompatible DNA end ligation by the XRCC4–DNA ligase IV complex: influence of terminal DNA sequence. *Nucleic Acids Res.* **35**, 5755–5762 (2007).
- Tsai, C. J., Kim, S. A. & Chu, G. Cernunnos/XLF promotes the ligation of mismatched and noncohesive DNA ends. *Proc. Natl Acad. Sci. USA* **104**, 7851–7856 (2007).
- Tadi, S. K. et al. PAXX is an accessory c-NHEJ factor that associates with Ku70 and has overlapping functions with XLF. *Cell Rep.* **17**, 541–555 (2016).

22. Riballo, E. et al. XLF-Cernunnos promotes DNA ligase IV-XRCC4 re-adenylation following ligation. *Nucleic Acids Res.* **37**, 482–492 (2009).
23. Mahaney, B. L., Hammel, M., Meek, K., Tainer, J. A. & Lees-Miller, S. P. XRCC4 and XLF form long helical protein filaments suitable for DNA end protection and alignment to facilitate DNA double strand break repair. *Biochem. Cell Biol.* **91**, 31–41 (2013).
24. Wu, Q. et al. Non-homologous end-joining partners in a helical dance: structural studies of XLF-XRCC4 interactions. *Biochem. Soc. Trans.* **39**, 1387–1392 (2011).
25. Andres, S. N. et al. A human XRCC4-XLF complex bridges DNA. *Nucleic Acids Res.* **40**, 1868–1878 (2012).
26. Brouwer, I. et al. Sliding sleeves of XRCC4-XLF bridge DNA and connect fragments of broken DNA. *Nature* **535**, 566–569 (2016).
27. Reid, D. A. et al. Organization and dynamics of the nonhomologous end-joining machinery during DNA double-strand break repair. *Proc. Natl Acad. Sci. USA* **112**, E2575–E2584 (2015).
28. Di Virgilio, M. & Gautier, J. Repair of double-strand breaks by nonhomologous end joining in the absence of Mre11. *J. Cell Biol.* **171**, 765–771 (2005).
29. Postow, L. et al. Ku80 removal from DNA through double strand break-induced ubiquitylation. *J. Cell Biol.* **182**, 467–479 (2008).
30. Labhart, P. Nonhomologous DNA end joining in cell-free systems. *Eur. J. Biochem.* **265**, 849–861 (1999).
31. Labhart, P. Ku-dependent nonhomologous DNA end joining in *Xenopus* egg extracts. *Mol. Cell. Biol.* **19**, 2585–2593 (1999).
32. Sandoval, A. & Labhart, P. Joining of DNA ends bearing non-matching 3'-overhangs. *DNA Repair (Amst.)* **1**, 397–410 (2002).
33. Taylor, E. M. et al. The Mre11/Rad50/Nbs1 complex functions in resection-based DNA end joining in *Xenopus laevis*. *Nucleic Acids Res.* **38**, 441–454 (2010).
34. Zhu, S. & Peng, A. Non-homologous end joining repair in *Xenopus* egg extract. *Sci. Rep.* **6**, 27797 (2016).
35. Thode, S., Schäfer, A., Pfeiffer, P. & Vielmetter, W. A novel pathway of DNA end-to-end joining. *Cell* **60**, 921–928 (1990).
36. Pfeiffer, P. & Vielmetter, W. Joining of nonhomologous DNA double strand breaks in vitro. *Nucleic Acids Res.* **16**, 907–924 (1988).
37. Graham, T. G. W., Walter, J. C. & Loparo, J. J. Ensemble and single-molecule analysis of non-homologous end joining in frog egg extracts. *Methods Enzymol* **591**, 233–270 (2017).
38. Graham, T. G. W., Walter, J. C. & Loparo, J. J. Two-stage synopsis of DNA ends during non-homologous end joining. *Mol. Cell* **61**, 850–858 (2016).
39. DeFazio, L. G., Stansel, R. M., Griffith, J. D. & Chu, G. Synopsis of DNA ends by DNA-dependent protein kinase. *EMBO J.* **21**, 3192–3200 (2002).
40. Hammel, M. et al. Ku and DNA-dependent protein kinase dynamic conformations and assembly regulate DNA binding and the initial non-homologous end joining complex. *J. Biol. Chem.* **285**, 1414–1423 (2010).
41. Cary, R. B. et al. DNA looping by Ku and the DNA-dependent protein kinase. *Proc. Natl Acad. Sci. USA* **94**, 4267–4272 (1997).
42. Spagnolo, L., Rivera-Calzada, A., Pearl, L. H. & Llorca, O. Three-dimensional structure of the human DNA-PKcs/Ku70/Ku80 complex assembled on DNA and its implications for DNA DSB repair. *Mol. Cell* **22**, 511–519 (2006).
43. Cottarel, J. et al. A noncatalytic function of the ligation complex during nonhomologous end joining. *J. Cell Biol.* **200**, 173–186 (2013).
44. Wang, J. L. et al. Dissection of DNA double-strand-break repair using novel single-molecule forceps. *Nat. Struct. Mol. Biol.* **25**, 482–487 (2018).
45. Normanno, D. et al. Mutational phospho-mimicry reveals a regulatory role for the XRCC4 and XLF C-terminal tails in modulating DNA bridging during classical non-homologous end joining. *eLife* **6**, e22900 (2017).
46. Lilliefors, H. W. On the Kolmogorov-Smirnov test for the exponential distribution with mean unknown. *J. Am. Stat. Assoc.* **64**, 387 (1969).
47. Fattah, F. J. et al. A role for XLF in DNA repair and recombination in human somatic cells. *DNA Repair (Amst.)* **15**, 39–53 (2014).
48. Ochi, T. et al. Structural insights into the role of domain flexibility in human DNA ligase IV. *Structure* **20**, 1212–1222 (2012).
49. Menon, V. & Povirk, L. F. XLF/Cernunnos: an important but puzzling participant in the nonhomologous end joining DNA repair pathway. *DNA Repair (Amst.)* **58**, 29–37 (2017).

Acknowledgements

We thank E. van Arnam (Harvard Medical School) for assistance with purification of Cy5 Halo ligand, B. Stinson (Harvard Medical School) for providing improved FRET analysis code and generating the pETDuet vector containing XRCC4 and LIG4, K. Schmitz (Massachusetts Institute of Technology) for advice on generating an 'orthogonal' codon-optimized XLF sequence, K. Arnett (HMS Center for Macromolecular Interactions) for assistance with biophysical assays, and S. Harrison and S. Jenni (Harvard Medical School) for assistance with dynamic light scattering. We would also like to thank members of the laboratories of J.J.L. and J.C.W. for helpful discussions. This work was funded by a National Institutes of Health grant R01GM115487 (to J.J.L.) and the Howard Hughes Medical Institute (J.C.W.).

Author contributions

All authors designed experiments and wrote the manuscript. T.G.W.G. and S.M.C. performed experiments and data analysis.

Competing interests

The authors declare no competing interests.

Additional information

Supplementary information is available for this paper at <https://doi.org/10.1038/s41594-018-0120-y>.

Reprints and permissions information is available at www.nature.com/reprints.

Correspondence and requests for materials should be addressed to J.J.L.

Publisher's note: Springer Nature remains neutral with regard to jurisdictional claims in published maps and institutional affiliations.

Methods

Plasmid construction. *XLF* and *XRCC4-LIG4* expression constructs. WT *X. laevis* XLF, XRCC4, and LIG4 plasmids were as previously described³⁸. A plasmid encoding human XRCC4 was obtained from Addgene (#13331) and was found to contain a single-nucleotide substitution resulting in the amino acid change I134T. This was restored to the reference sequence by site-directed mutagenesis, and the XRCC4 coding sequence was subcloned into a H10-SUMO expression vector. For human XLF, a bacterial codon-optimized gene block (Integrated DNA Technologies) was cloned into a H10-SUMO expression vector. Point mutants, epitope-tagged proteins, and C-terminally truncated XLF₁₋₂₂₆ were generated by standard round the horn site-directed mutagenesis⁵⁰. An H10-SUMO-Halo-XLF expression plasmid was created by isothermal assembly of a Halo-encoding fragment and a PCR product of the original H10-SUMO-XLF plasmid. A dual expression vector for XRCC4 and H6-SUMO-LIG4^{K278R} was constructed by amplifying XRCC4, H6-SUMO, and LIG4 from previously described plasmids³⁸, and inserting the fragments in a pETDuet vector by isothermal assembly. All constructs were verified by Sanger sequencing.

Tandem XLF dimer. A custom Python script was used to generate a second codon-optimized XLF sequence (XLF') as dissimilar as possible from our existing codon-optimized XLF sequence, to facilitate cloning and to prevent recombination between the two XLF sequences. Additional sequence encoding the linker GGGSGGGSGGGSGGG was appended at the 3' end of the XLF' sequence, and this combined fragment was ordered as a gBlock from Integrated DNA Technologies, inserted into a cloning vector, and sequence verified. The XLF' + linker sequence was then inserted by isothermal assembly immediately upstream of the initial XLF methionine in H10-SUMO-XLF³⁸, thus yielding the tandem dimer H10-SUMO-XLF'-linker-XLF.

XLF heterodimers. A plasmid for expression of H10-tagged XLF (pTG355) was created by using round-the-horn mutagenesis to delete the SUMO tag in H10-SUMO-XLF (pTG296). The alternative codon-optimized XLF sequence described above was inserted together with a T7 promoter and an N-terminal Flag-Avitag sequence into the H10-XLF plasmid, thereby generating a vector for dual expression of two versions of XLF with different affinity tags.

Protein purification. *XLF*. Plasmids encoding H10-SUMO-tagged WT XLF and XLF point mutants were transformed into *Escherichia coli* BL21(DE3)pLysS cells. Cultures were grown in LB medium at 37°C to an OD₆₀₀ of ~0.6, IPTG was added to a final concentration of 1 mM to induce expression, and cultures were grown an additional 3 h at 25–30°C. Cells were collected by centrifugation, and cell pellets were flash-frozen in liquid nitrogen and stored at –80°C. H10-SUMO-tagged proteins were purified essentially as described previously⁵¹. Briefly, cells were lysed by sonication in His-SUMO lysis buffer (20 mM Tris-HCl, pH 8, 1 M NaCl, 30 mM imidazole, 5 mM BME, and 1 mM PMSF), and lysates were clarified by centrifugation for 1 h at 25,000 r.p.m. in an SW-41 rotor at 4°C. Clarified lysates were incubated with Ni-NTA-agarose (Qiagen) for 1 h at 4°C to bind histidine-tagged proteins. Ni-NTA resin was washed extensively with lysis buffer followed by 'salt-reduction' buffer (20 mM Tris-HCl, pH 8, 350 mM NaCl, 30 mM imidazole, and 5 mM BME). Protein was eluted with elution buffer (20 mM Tris-HCl, pH 8, 350 mM NaCl, 300 mM imidazole, and 5 mM BME). Peak elution fractions were pooled, H6-tagged Ulp1 protease was added to cleave the H10-SUMO tag, and the protein was dialyzed overnight against His-SUMO dialysis buffer (20 mM Tris-HCl, pH 8, 350 mM NaCl, 10% glycerol, 10 mM imidazole, and 5 mM BME). The dialysate was then incubated again with Ni-NTA resin for 1.5 h at 4°C to remove H10-SUMO, uncleaved H10-SUMO-XLF, and H6-Ulp1. The flow through (containing untagged XLF) was collected and diluted with 1.36 volumes of SP buffer A (50 mM Na-MES, pH 6.5, 10% glycerol, and 1 mM DTT) and passed over SP Sepharose Fast Flow (Amersham) equilibrated with SP buffer A + 150 mM NaCl. The resin was washed with SP buffer A + 150 mM NaCl, and protein was eluted with SP buffer A + 300 mM NaCl. Protein aliquots in this buffer were flash-frozen in liquid nitrogen and stored at –80°C.

Halo-XLF. Halo-XLF was expressed as a H10-SUMO fusion and subjected to Ni-NTA purification as described for H10-SUMO-XLF above. The flow through after the second Ni-NTA step was subjected to size-exclusion purification on a HiPrep Sephacryl S-200 26/60 High Resolution column equilibrated with His-SUMO dialysis buffer (20 mM Tris-HCl, pH 8, 350 mM NaCl, 10% glycerol, 10 mM imidazole, and 5 mM BME). Peak fractions were pooled and concentrated on a 15-ml 10-kDa molecular-weight cutoff (MWCO) centrifugal concentrator.

XLF¹⁻²²⁶ truncation mutant. XLF truncation mutants were expressed as fusions to H10-SUMO in BL21(DE3)pLysS cells and subjected to the same initial His-SUMO purification protocol used for full-length XLF. Flow through from the second Ni-NTA step was diluted with approximately 2.5 volumes of 20 mM Tris-HCl, pH 8, 10% glycerol, and 5 mM BME to decrease the NaCl concentration to ~100 mM. The diluted sample was passed over a Mono Q column equilibrated with 20 mM Tris-HCl, pH 8, 100 mM NaCl, 10% glycerol, and 5 mM BME. The flow through, containing the protein of interest, was concentrated with an Amicon 10-kDa

MWCO centrifugal concentrator and dialyzed overnight against 20 mM Tris-HCl, pH 8, 350 mM NaCl, 10% glycerol, and 5 mM BME. Human XLF¹⁻²²⁴ was purified through the same protocol. However, it bound the MonoQ column and was eluted with a NaCl gradient of 100–1,000 mM.

XLF tandem dimer. XLF tandem dimer constructs were expressed as fusions to H10-SUMO in BL21(DE3)pLysS cells and subjected to the His-SUMO purification described above for WT XLF. Flow through from the second Ni-NTA step was diluted with 1.36 volumes of buffer A (50 mM Na-MES, pH 6.5, 10% glycerol, and 5 mM BME) and bound to a HiTrap SP HP column equilibrated with the same buffer containing 150 mM NaCl. The protein was eluted with a gradient of 150 mM to 1 M NaCl over 20 column volumes (CV). Peak fractions were pooled, concentrated on a 10-kDa MWCO Amicon centrifugal concentrator, and subjected to size-exclusion purification on a Superdex 200 Increase 10/300 column equilibrated with 50 mM Na-MES, pH 6.5, 350 mM NaCl, 10% glycerol, and 5 mM BME. Peak fractions were pooled and concentrated as described above.

XLF heterodimers. BL21(DE3) cells were cotransformed with the BirA biotin ligase expression plasmid pBirAcm and a dual-expression plasmid encoding H10-XLF as well as Flag-Avitag-XLF^{WT} (pTG448) or Flag-Avitag-XLF^{E117D} (pTG449). After the cells had grown to an OD₆₀₀ of 0.4, expression was induced by addition of IPTG to 1 mM, and the growth medium was supplemented with biotin to a final concentration of 25 µM. Cells were collected by centrifugation after 3 h of induction at 25–30°C, flash-frozen, and stored at –80°C. Frozen cell pellets were resuspended in 20 mM Tris-HCl, pH 8, 1 M NaCl, 30 mM imidazole, and 5 mM BME and lysed by three 30-s cycles of sonication (1 s on, 1 s off). Lysates were clarified by centrifugation for 1 h at 25,000 r.p.m. in an SW-41 rotor. Supernatants were incubated for 1 h at 4°C with 250 µl of Ni-NTA agarose (Qiagen) per liter of culture. Resin was washed with 40 CV of lysis buffer, and H10-tagged complexes were eluted with 20 CV of the same buffer containing 300 mM imidazole. Next, eluates were passed by gravity flow over SoftLink Avidin resin (Promega; 1 ml per liter of culture) to capture Avitagged H10-XLF-Flag-Avitag-XLF heterodimers. The resin was washed with 25 CV of 20 mM Tris-HCl, pH 8, 1 M NaCl, and 5 mM BME, followed by 5 CV of 20 mM Tris-HCl, pH 8, 350 mM NaCl, and 5 mM BME. We suspect that the use of high-salt buffers at this stage is important to remove nonspecifically bound H10-XLF^{WT}-H10-XLF^{WT} homodimer, because early WT-mutant heterodimer preparations purified under less stringent conditions exhibited variable and elevated activity (data not shown). Bound protein was eluted in 1-CV increments with 20 mM Tris-HCl, pH 8, 350 mM NaCl, 5 mM BME, and 5 mM biotin, with a pause of at least 5 min between elution steps to facilitate dissociation of bound protein. Protein was flash-frozen and stored at –80°C in elution buffer.

XRCC4. N-terminal H10-SUMO fusion constructs of *X. laevis* XRCC4 were transformed into BL21(DE3)pLysS *E. coli* cells. The cells were grown at 37°C to an OD₆₀₀ of 0.6 and then induced with 1 mM IPTG for 3 h at ~25–30°C. Cells were pelleted by centrifugation, flash frozen, and stored at –80°C. Cell pellets were then thawed and subjected to the His-SUMO purification used previously³⁸.

Biotinylated XRCC4-Avitag. *X. laevis* XRCC4 with an N-terminal H10-SUMO tag and a C-terminal Avitag was expressed in BL21(DE3) *E. coli* cells cotransformed with the BirA biotin ligase-expressing plasmid pBirAcm. Cells were grown in LB medium supplemented with 100 µM biotin, and protein expression was induced with 1 mM IPTG for 3 h at ~25–30°C. Protein was subjected to the same initial H10-SUMO purification steps used for XLF (described above). Biotinylated protein was then bound to SoftLink Avidin resin equilibrated with 20 mM Tris-HCl, pH 8, 150 mM NaCl, 10% glycerol, and 1 mM DTT. The resin was washed with 20 CV of the same buffer, and protein was eluted with elution buffer (20 mM Tris-HCl, pH 8, 150 mM NaCl, 10% glycerol, 1 mM DTT, and 5 mM biotin). Elution was performed in increments of 2 CV, with a pause of 5 min between elutions. Peak fractions were pooled and dialyzed overnight against 20 mM Tris-HCl, pH 8, 350 mM NaCl, 10% glycerol, and 1 mM DTT. Human XRCC4-Avitag was purified with the same protocol.

XRCC4-LIG4 complex. WT and mutant XRCC4-LIG4 complexes were expressed in Sf9 cells and purified as described previously³⁸. Catalytically inactive XRCC4-LIG4^{K278R} complexes (for the experiments in Fig. 2d,e) were expressed from a pETDuet vector in Rosetta 2 (DE3) *E. coli* cells. Cultures were grown at 37°C to an OD₆₀₀ of 0.6 and then placed on ice for 20 min. IPTG was added to a final concentration of 1 mM, and cultures were incubated with shaking for 16 h at 17°C. Cells were pelleted by centrifugation, flash frozen, and stored at –80°C. Cell pellets were thawed and resuspended in 20 ml of lysis buffer (20 mM HEPES, pH 7.5, 400 mM NaCl, 20 mM imidazole, 10% glycerol, 1 mM DTT, and one cOmplete, EDTA-free Protease Inhibitor tablet (Sigma Aldrich)) per liter of culture. The resuspension was sonicated for 2 min (5 s on, 10 s off). Lysates were clarified by 1 h of centrifugation at 38,724 r.c.f. at 4°C. The lysates were then incubated at 4°C for 1 h with 250 µl of Ni-NTA agarose (Qiagen) per liter of culture. The samples were centrifuged at 500 r.c.f., the supernatant was discarded, and the Ni-NTA resin was resuspended in 10 ml of lysis buffer and poured into a gravity-flow column. The resin was then washed with 20 ml of lysis buffer, and protein was eluted in 250-µl

fractions with lysis buffer containing 250 mM imidazole. Fractions containing the protein of interest were pooled, supplemented with Ulp1 protease, and dialyzed into cleavage buffer (20 mM HEPES, pH 7.5, 150 mM NaCl, 1 mM DTT, and 10% glycerol). The dialyzed sample was then incubated with 250 μ l of Ni-NTA resin per liter of culture for 1.5 h at 4°C. The flow through was collected, passed through a 0.22 μ m filter, and diluted in cleavage buffer without NaCl to bring the final NaCl concentration to 50 mM. Protein was bound to a MonoQ 5/50-GI column (GE Healthcare Life Sciences) equilibrated in buffer A (cleavage buffer with 50 mM NaCl) and eluted with a 20-ml gradient of 0–60% buffer B (cleavage buffer with 1 M NaCl). Peak fractions were pooled and further separated on a S200 16/600 200-pg sizing column (GE Healthcare Life Sciences) equilibrated with cleavage buffer. Protein-containing fractions were pooled and concentrated with an Amicon 10-kDa MWCO centrifugal concentrator.

Biotin-Avitag-Halo. N-terminally SUMO-tagged Avitag-Halo protein was expressed in BL21(DE3) cells containing the pBirAcm plasmid, which encodes the BirA biotin ligase. It was subjected to the same His-SUMO purification procedure used for XLF, without the final ion-exchange step.

Flag-XLF and H10-XLF (for monomer-exchange experiments). A Flag-XLF expression plasmid was transformed into BL21(DE3) pLysS cells, which were grown in 100 ml of LB to an OD₆₀₀ of 0.4, induced with 1 mM IPTG for 3 h at 25–30°C, and collected by centrifugation. Cells were lysed in 20 mM Tris-HCl, pH 7.5, and 150 mM NaCl, without reducing agent. The lysate was clarified by centrifugation at 16,000 r.c.f. in a 4°C microcentrifuge and incubated with 50 μ l of anti-Flag M2 affinity gel (Sigma-Aldrich) for 1 h at 4°C. The gel was washed three times with 1.4 ml of lysis buffer, and protein was eluted by overnight incubation at 4°C with 100 μ g/ μ l of 3 \times Flag peptide (Sigma-Aldrich). Protein was dialyzed against storage buffer (20 mM Tris-HCl, pH 7.5, 150 mM NaCl, 10% glycerol, and 5 mM BME) with a 7-kDa MWCO dialysis cassette, divided into aliquots, flash-frozen, and stored at –80°C. H10-XLF was expressed in BL21(DE3) pLysS cells under the same growth and induction conditions used for H10-SUMO-XLF. Initial Ni-NTA purification followed the same steps as for H10-SUMO-XLF. The protein was dialyzed overnight against 20 mM Na-MES, pH 6.5, 150 mM NaCl, 10% glycerol, and 5 mM BME; bound to a Mono S column; and eluted with a gradient of the same buffer with 150 mM to 1 M NaCl. Peak fractions were pooled and dialyzed overnight against 20 mM Tris-HCl, pH 7.5, 350 mM NaCl, 10% glycerol, and 1 mM DTT. Protein was concentrated with a centrifugal concentrator, divided into aliquots, flash-frozen, and stored at –80°C.

Test of monomer exchange between XLF dimers. To assess whether monomers are exchanged between XLF dimers in solution (Supplementary Fig. 4d), we mixed N-terminally Flag- and H10-tagged XLF proteins at final concentrations of 8 μ M and 20 μ M, respectively, in a 5- μ l volume of 20 mM Tris-HCl, pH 7.5, 250 mM NaCl, 10% glycerol, 2.5 mM BME, and 0.5 mM DTT. Control reactions contained only one protein or the other. Reactions were incubated for 3 h at room temperature in a humidified chamber. 100 μ l of His-SUMO lysis buffer was added (20 mM Tris-HCl, pH 8, 1 M NaCl, 30 mM imidazole, and 5 mM BME), and tubes were centrifuged for 10 min at 16,000 r.c.f. in a 4°C microcentrifuge. No pellet was visible. After 15 μ l of supernatant was withdrawn for analysis, 80 μ l of supernatant was incubated for 1 h at 4°C with 10 μ l of Ni-NTA-agarose resin prewashed with His-SUMO lysis buffer. Supernatant was collected, and the resin was washed twice with 500 μ l of His-SUMO lysis buffer, with thorough aspiration after each wash. 80 μ l of His-SUMO elution buffer was added (20 mM Tris-HCl, pH 8, 350 mM NaCl, 300 mM imidazole, and 5 mM BME), and protein was eluted for 30 min at 4°C. Input, supernatant, and eluate samples were separated on a 4–15% precast SDS-PAGE gel (Bio-Rad), transferred to polyvinylidene fluoride membranes for 1 h at 100 V at 4°C, and blocked with 5% powdered nonfat milk in PBST (1 \times phosphate-buffered saline with 0.05% Tween 20). Membranes were probed overnight with 1:5,000 anti-H6 (Sigma-Aldrich) or 1:5,000 anti-FLAG M2 (Sigma-Aldrich), washed three times with PBST, and probed for 1 h with 1:20,000 horseradish peroxidase-conjugated rabbit anti-mouse IgG (H + L) secondary antibody (Jackson ImmunoResearch 315-035-003). After being washed again three times with PBST, the anti-H6 blot was incubated with chemiluminescent horseradish peroxidase substrate (HyGLO Quick Spray, Denville Scientific), and the anti-Flag blot was incubated with enhanced chemiluminescent substrate (Pierce). Both blots were imaged on an Amersham Imager 600 (GE Healthcare Life Sciences).

Preparation of sulfo-Cy5-Halo substrate. 8 μ l of 100 mM Cy5-NHS ester in DMSO was combined with 3.2 μ l of 250 mM HaloTag amine (O2) ligand (Promega) and 38.8 μ l of 100 mM sodium bicarbonate and allowed to react overnight. The products were separated by reversed-phase HPLC on a semipreparative C18 column with a gradient of 20–100% acetonitrile in water. Product identity was verified by mass spectrometry. Peaks corresponding to the correct product were pooled, and solvent was evaporated overnight with a SpeedVac concentrator. The compound was redissolved in DMSO, and the concentration was determined according to the absorbance at 650 nm of a 1:100 dilution in water, assuming an extinction coefficient of 250,000 M^{–1} cm^{–1} for Cy5.

Fluorescence labeling of Halo-XLF. A twofold molar excess of Cy5- or Alexa Fluor 488-Halo ligand in DMSO was added to Halo-XLF protein in its storage buffer. The mixture was allowed to react for 10 min while being centrifuged at 16,000 r.c.f. at room temperature. Labeled protein was separated from free dye on a Superdex 200 Increase 10/300 column equilibrated with 20 mM Tris-HCl, pH 8, 350 mM NaCl, 10% glycerol, and 5% β -mercaptoethanol. Peak fractions were pooled and concentrated with an Amicon 10-kDa MWCO centrifugal concentrator. Protein concentrations were measured on the basis of absorbance at 280 nm, assuming an extinction coefficient of 82,390 M^{–1} cm^{–1}. Dye concentrations were measured according to absorbance at 650 nm for Cy5 (assuming an extinction coefficient of 250,000 M^{–1} cm^{–1}) or 495 nm for AF488 (assuming an extinction coefficient of 73,000 M^{–1} cm^{–1}). For AF488-labeled protein, the absorbance at 280 nm due to protein was determined by subtraction of the AF488 absorbance at 280 nm from the total absorbance, with the correction factor (AF488 absorbance at 280 nm) = 0.11 \times (AF488 absorbance at 495 nm). The labeled fraction of monomer was obtained by division of the molar concentration of dye by the molar concentration of protein. Measurements of the labeled fraction obtained with a NanoDrop spectrophotometer agreed with those calculated from dual-wavelength absorbance measurements of labeled protein peaks during size-exclusion chromatography.

Fluorescence labeling of XLF with Cy5-maleimide. 130 μ l of 53 μ M WT *X. laevis* XLF was incubated for 1 h at room temperature with 50 μ M sulfo-Cy5 maleimide (Lumiprobe) in 20 mM Tris-HCl, pH 7.5, 350 mM NaCl, and 10% glycerol. The labeling reaction was quenched by the addition of DTT at a final concentration of 5 mM. Labeled protein was separated from free dye on a S200 Increase 10/300 GL sizing column (GE Healthcare Life Sciences). Protein-containing fractions were collected, and the Cy5:XLF ratio was determined according to the absorbance of each, measured with a NanoDrop spectrophotometer. With an extinction coefficient of 250,000 M^{–1} cm^{–1} for Cy5 and an extinction coefficient of 24,450 M^{–1} cm^{–1} for XLF, the dye-to-protein ratio was measured to be 0.77. This same procedure was performed in parallel for an AF488-labeled XLF sample and a mock-labeled XLF sample.

Preparation of *Xenopus* egg extracts. *Xenopus* egg extract was prepared as previously described³². The female frogs used to produce oocytes were cared for by the Center for Animal Resources and Comparative Medicine at Harvard Medical School (AAALAC accredited). Work performed for this study was in accordance with the rules and regulations set by AAALAC. The Institutional Animal Care and Use Committee (IACUC) of Harvard Medical School approved the work.

Antibodies and immunodepletion. XLF and XRCC4 antibodies were the same as described previously³⁸. Immunodepletion experiments were performed as described previously^{37,38}. For rescue experiments in Figs. 1c,d and 5b, immunodepleted extract was supplemented with 500 nM XLF or 50 nM XRCC4-LIG4 complex.

Bulk end-joining assays. Bulk end-joining assays were performed as described previously³⁸. The final concentration of radiolabeled linear substrate DNA in bulk end joining assays was approximately 1 ng/ μ l (~0.5 nM). The integrated intensity of gel bands (Fig. 4c and Supplementary Fig. 4f) was quantified in Fiji.

tdXLF and XLF heterodimer titration experiments. To test the dependence of the end-joining rate on the protein concentration of XLF tandem dimer (tdXLF; Fig. 4b–d) and heterodimer (Supplementary Fig. 4e,f) constructs, we depleted extract of endogenous XLF, then supplemented the depleted extract with an ATP-regeneration system and closed-circular carrier DNA, as described previously³⁷. Radiolabeled linear substrate DNA was added to extract on ice to a final concentration of ~1 ng/ μ l, and a portion of this extract mixture was supplemented with XLF at the indicated maximum concentration. The same fractional volume of XLF storage buffer was added to the remaining extract mixture. Extract supplemented with XLF was then serially diluted with extract mixture, while tubes were kept in a PCR block at 0°C. After serial dilutions, the temperature of the block was raised to 22°C for 5 min, then lowered to 0°C to stop the reactions. One volume of reaction stop solution/loading dye with proteinase K³⁷ was immediately added to all tubes. Products were analyzed by gel electrophoresis as described previously³⁷.

Microscope and flow-cell construction. Samples were imaged with a through-objective TIRF microscope built around an Olympus IX-71 inverted microscope body. 488-nm, 532-nm, and 641-nm laser beams (Coherent Sapphire 488, Coherent Sapphire 532, and Cube 641, respectively) were expanded, combined with dichroic mirrors, expanded again, and focused on the rear focal plane of an oil-immersion objective (Olympus UPlanSApo, 100 \times ; NA, 1.40). The focusing lens was placed on a vertical translation stage to permit manual adjustment of the TIRF angle. Emission light was separated from excitation light with a multipass dichroic mirror, and laser lines were further attenuated with a StopLine 488/532/635 notch filter (Semrock). A home-built beamsplitter (ref. ³⁷) was used to separate Alexa Fluor 488 and Cy3 emission from Cy5 emission; these two channels were imaged on separate halves of an electron-multiplying charge-coupled device camera

(Hamamatsu, ImageEM 9100-13), which was operated at maximum EM gain. An automated microstage (Mad City Labs) was used to position the sample and move between fields of view.

Coverslips were functionalized with a mixture of methoxypolyethylene glycol (mPEG) and biotin-mPEG, and flow cells were constructed according to a previously described protocol^{38,53}.

Single-molecule imaging and analysis. Single-molecule imaging and analysis is described in the Supplementary Note.

Biolayer interferometry binding assays. BLI experiments were performed on an Octet RED384 (ForteBio) with streptavidin-coated Dip and Read Biosensors (ForteBio) and 384-well plates. 100 nM of biotinylated C-terminally Avi-tagged XRCC4 was bound for 5 min in a binding buffer consisting of 20 mM Tris-HCl, pH 7.5, 125 mM KCl, 10 mg/mL bovine serum albumin (Calbiochem), and 5 mM BME. To test for nonspecific binding of XLF^{1–226}, reference tips were incubated in buffer alone. The tips were washed with buffer for 60 s to obtain a baseline reading and then transferred to wells containing XLF^{1–226} or point mutants thereof (2 μ M of each protein unless otherwise noted) for 120 s. After measurement of association, the tips were moved to wells containing buffer, and XLF dissociation was measured for 180 s. The response for each experimental condition shown in Fig. 1a is the average of three replicates, and each replicate is the average of three sequential rounds of association and dissociation. The s.d. is represented as shading around each trace. The data shown in Supplementary Fig. 1a are representative results from a single experiment. For the titration experiments shown in Supplementary Fig. 1b,e,f, the background subtracted association-dissociation curve for each concentration was fit to a 1:1 model with GraphPad Prism software and the built-in fitting tools. Data generated from fits for which $R^2 < 0.98$ were not included in subsequent analysis. The resulting k_{on} , k_{off} , and apparent K_d values were averaged. This procedure was performed for two replicates for each condition. The reported values are averages from the two replicates, and the reported error represents the minimum and maximum values. The same fitting and analysis procedure was used to generate the curves shown in Fig. 5c and the values in Supplementary Table 1. Those data represent two experimental replicates, with the error representing the minimum and maximum values.

Dynamic light scattering. DLS experiments were performed on a Wyatt/Protein Solutions DynaPro-99-E-50 Dynamic Light Scattering Module with a TC100-830 Temperature Controlled Microsampler. The data shown in Supplementary Fig. 1c,i were collected at 20 °C with an acquisition time of 10 s and a read interval of 1 s. Sample measurement began ~1 min after assembly and mixing of the specified proteins in a filtered buffer containing 20 mM HEPES, pH 8, 75 mM KCl, 0.5 mM EDTA, 1 mM DTT, and 5% glycerol. Dynamics V6 software (Wyatt/Protein Solutions) was used to calculate hydrodynamic radii with the built-in parameters for a 5% glycerol solution. For each condition, three replicates were averaged to generate the data shown in Supplementary Fig. 1c,i. The shaded region around each trace represents the s.e.m.

Bulk protein–DNA pulldown assays. DNA pulldown assays (Supplementary Figs. 1d,h and 3e) were performed as previously described²⁵. A biotinylated 1,000-bp DNA fragment was generated by PCR (template pTG064; primers oTG414 and oTG042F) with Pfu polymerase. The 500-bp DNA was generated by PvuII digestion of pTG024. These DNA substrates were then gel-purified by electroelution, as described previously³⁷. M-280 streptavidin-coated magnetic Dynabeads (Thermo Fisher Scientific) were washed three times with one volume of binding buffer (20 mM HEPES, pH 8, 75 mM KCl, 0.5 mM EDTA, 1 mM DTT, 5% glycerol, and 400 μ g/mL BSA (New England Biolabs)), with a magnet to retain beads, then resuspended in one volume of the same buffer. Beads were incubated with 1,000-bp DNA at a final concentration of 20 ng/ μ L for 5 min at 20–25 °C. One volume of high-salt buffer (binding buffer with 850 mM KCl) was used to wash the beads twice before resuspension in wash buffer. The 500-bp DNA was then added at a final concentration of 20 ng/ μ L. 10 μ L of the bead–DNA suspension was added to each 40- μ L reaction assembled in binding buffer. The indicated proteins were added at a final concentration of 2 μ M, and the reactions were incubated at room temperature for 30 min. After a magnet was used to capture the beads, the supernatant was collected, and the beads were then washed twice in binding buffer and resuspended in the same buffer without BSA. 10 μ L of each sample was set aside and separated on a 4–15% SDS-PAGE gel (Bio-Rad). An Amersham Imager

600 was used to visualize Cy5-labeled XLF. The samples were then treated with 40 ng proteinase K for 1 h at 50 °C, and DNA was separated on a 1.5% agarose gel.

Differential scanning fluorimetry. Differential scanning fluorimetry protein thermal-shift assays were performed with a QuantStudio 6 Flex Real-Time PCR System (Applied Biosystems). 20- μ L reactions containing 10 μ g of the specified protein were assembled in MicroAmp FAST optical 96-well reaction plates (Life Technologies) and covered with MicroAmp Optical Adhesive Film (Life Technologies). SYPRO Orange dye was included in the reactions with a Protein Thermal Shift Dye Kit (Applied Biosystems), according to the manufacturer's instructions. Protein samples were diluted in storage buffer (20 mM Tris-HCl, pH 8, 10 mM imidazole, 350 mM NaCl, and 10% glycerol). The temperature was raised from 25 to 99 °C at 3 °C per minute, and the fluorescent dye was excited and measured at 470 nm and 587 nm, respectively. To determine the melting temperatures, we plotted emission signals as a function of temperature, and these thermal denaturation curves were fit with the Boltzmann equation in Protein Thermal Shift software (Life Technologies). The average of three experimental replicates is shown for each condition. The error bars represent the s.e.m. A two-tailed, unpaired *t* test with unequal variance was performed to determine whether the melting temperatures of the mutants were significantly different from those of the WT proteins.

Size-exclusion chromatography with multiangle light scattering. SEC–MALS was performed on an Agilent 1260 Infinity Isocratic Liquid Chromatography System equipped with a Wyatt Dawn Heleos II Multi-Angle Light Scattering detector and a Wyatt Optilab T-rex Refractive Index Detector. An Agilent AdvanceBio 300 column was pre-equilibrated overnight with running buffer (50 mM Na-MES, pH 6.5, 350 mM NaCl, 10% glycerol, and 5 mM BME) at a 0.2 mL/min flow rate and then allowed to equilibrate to a flow rate of 0.4 mL/min for 1 h. 30 μ L of a 50 μ M solution of tdXLF^{WT/WT} was separated on the column. As a control, 100 μ L of 2 mg/mL BSA fraction V (OmniPur) in the same buffer without BME was separated on the column, thus yielding monomer, dimer, and trimer peaks of the expected sizes.

Statistics and reproducibility. A two-tailed unpaired *t* test with unequal variances was used to determine significance ($P < 0.05$) in Supplementary Fig. 1e–g. Bonferroni correction was applied in the case of Supplementary Fig. 1g. A log-rank test was used to determine significance ($P < 0.05$) in Fig. 2e. The Lilliefors test for exponential distribution (MATLAB function 'lillietest') was applied to the data shown in Fig. 2e. For figures that include representative images, the number of experimental replicates of the corresponding experiments are: two for Fig. 1c,d, three for Fig. 3b,c, three for Fig. 5a, two for Fig. 5b, two for Supplementary Fig. 1a, two for Supplementary Fig. 2b, three for Supplementary Fig. 1d, two for Supplementary Fig. 1h, five for Supplementary Fig. 2a, two for Supplementary Fig. 3d, two for Supplementary Fig. 3e, two for Supplementary Fig. 4d, and six for Supplementary Fig. 4e,f. The exact experimental conditions were varied slightly between replicates of some experiments, and appropriate internal controls were used in all cases. Similar results were obtained among replicates for all experiments listed above.

Reporting Summary. Further information on research design is available in the Nature Research Reporting Summary linked to this article.

Data availability

The data that support the findings of this study and the custom-written computer code used to analyze them are available from the corresponding author upon reasonable request. Source data for Figs. 2b,c, 4c, and 5c are available with the paper online.

References

- Hemsley, A., Arnheim, N., Toney, M. D., Cortopassi, G. & Galas, D. J. A simple method for site-directed mutagenesis using the polymerase chain reaction. *Nucleic Acids Res.* **17**, 6545–6551 (1989).
- Graham, T. G. W. et al. ParB spreading requires DNA bridging. *Genes Dev.* **28**, 1228–1238 (2014).
- Lebofsky, R., Takahashi, T. & Walter, J. C. DNA replication in nucleus-free *Xenopus* egg extracts. *Methods Mol. Biol.* **521**, 229–252 (2009).
- Tanner, N. A. et al. Single-molecule studies of fork dynamics in *Escherichia coli* DNA replication. *Nat. Struct. Mol. Biol.* **15**, 998 (2008).

Reporting Summary

Nature Research wishes to improve the reproducibility of the work that we publish. This form provides structure for consistency and transparency in reporting. For further information on Nature Research policies, see [Authors & Referees](#) and the [Editorial Policy Checklist](#).

Statistical parameters

When statistical analyses are reported, confirm that the following items are present in the relevant location (e.g. figure legend, table legend, main text, or Methods section).

n/a Confirmed

- ☐ ☒ The exact sample size (n) for each experimental group/condition, given as a discrete number and unit of measurement
- ☒ ☐ An indication of whether measurements were taken from distinct samples or whether the same sample was measured repeatedly
- ☐ ☒ The statistical test(s) used AND whether they are one- or two-sided
Only common tests should be described solely by name; describe more complex techniques in the Methods section.
- ☒ ☐ A description of all covariates tested
- ☐ ☒ A description of any assumptions or corrections, such as tests of normality and adjustment for multiple comparisons
- ☐ ☒ A full description of the statistics including central tendency (e.g. means) or other basic estimates (e.g. regression coefficient) AND variation (e.g. standard deviation) or associated estimates of uncertainty (e.g. confidence intervals)
- ☐ ☒ For null hypothesis testing, the test statistic (e.g. F , t , r) with confidence intervals, effect sizes, degrees of freedom and P value noted
Give P values as exact values whenever suitable.
- ☒ ☐ For Bayesian analysis, information on the choice of priors and Markov chain Monte Carlo settings
- ☒ ☐ For hierarchical and complex designs, identification of the appropriate level for tests and full reporting of outcomes
- ☒ ☐ Estimates of effect sizes (e.g. Cohen's d , Pearson's r), indicating how they were calculated
- ☐ ☒ Clearly defined error bars
State explicitly what error bars represent (e.g. SD, SE, CI)

Our web collection on [statistics for biologists](#) may be useful.

Software and code

Policy information about [availability of computer code](#)

Data collection

The collection of all single-molecule data is described in the Methods section under 'Single-molecule imaging and analysis'. ForteBio Octet 384 Data Acquisition 9.0 software was used collect all bio-layer interferometry data. Wyatt/Protein Solutions Dynamics V6 software was used to collect dynamic light scattering data. Life Technologies Protein Thermal Shift software was used to collect differential scanning fluorimetry data.

Data analysis

The software used and analysis of all single-molecule data is described in the Methods section under 'Single-molecule imaging and analysis'. ForteBio Octet 384 Data Analysis 8.0 software and GraphPad Prism software were used analyze all bio-layer interferometry data as described in the Methods section under 'Bio-layer interferometry (BLI) binding assays'. Wyatt/Protein Solutions Dynamics V6 software was used to analyze dynamic light scattering data as described in the Methods section under 'Dynamic light scattering'. Life Technologies Protein Thermal Shift software was used to analyze differential scanning fluorimetry data as described in the Methods section under 'Differential scanning fluorimetry'. Results from gel-based assays were quantified using Fiji.

For manuscripts utilizing custom algorithms or software that are central to the research but not yet described in published literature, software must be made available to editors/reviewers upon request. We strongly encourage code deposition in a community repository (e.g. GitHub). See the Nature Research [guidelines for submitting code & software](#) for further information.

Data

Policy information about [availability of data](#)

All manuscripts must include a [data availability statement](#). This statement should provide the following information, where applicable:

- Accession codes, unique identifiers, or web links for publicly available datasets
- A list of figures that have associated raw data
- A description of any restrictions on data availability

The data that support the findings of this study and the custom-written computer code used to analyze it are available from the corresponding author upon reasonable request.

Field-specific reporting

Please select the best fit for your research. If you are not sure, read the appropriate sections before making your selection.

☒ Life sciences ☐ Behavioural & social sciences ☐ Ecological, evolutionary & environmental sciences

For a reference copy of the document with all sections, see [nature.com/authors/policies/ReportingSummary-flat.pdf](https://www.nature.com/authors/policies/ReportingSummary-flat.pdf)

Life sciences study design

All studies must disclose on these points even when the disclosure is negative.

Sample size	Sample sizes for all datasets are listed in the figure captions, the associated Methods section, or in Supplementary tables. Generally, samples sizes were chosen to reliably reproduce experimental observations within reasonable margins of error.
Data exclusions	BLI response curves for which fitting to a 1:1 model as described in the Methods section, 'Bio-layer interferometry (BLI) binding assays' generated R-square values less than 0.98 were not included in subsequent analysis. Poor fitting to this model only occurred at very low concentrations of the protein being titrated where the measurable response was minimal. For single-molecule data analysis, spots were excluded if they showed evidence of containing more than one DNA substrate. Details are provided in the Methods.
Replication	All data have been successfully reproduced. The number of replicates and associated error are noted in the Methods section, figures, figure captions, main text, and/or Supplementary tables.
Randomization	Randomization was not relevant to this study.
Blinding	Blinding was not relevant to this study.

Reporting for specific materials, systems and methods

Materials & experimental systems

n/a	Involved in the study
<input type="checkbox"/>	<input checked="" type="checkbox"/> Unique biological materials
<input type="checkbox"/>	<input checked="" type="checkbox"/> Antibodies
<input checked="" type="checkbox"/>	<input type="checkbox"/> Eukaryotic cell lines
<input checked="" type="checkbox"/>	<input type="checkbox"/> Palaeontology
<input type="checkbox"/>	<input checked="" type="checkbox"/> Animals and other organisms
<input checked="" type="checkbox"/>	<input type="checkbox"/> Human research participants

Methods

n/a	Involved in the study
<input checked="" type="checkbox"/>	<input type="checkbox"/> ChIP-seq
<input checked="" type="checkbox"/>	<input type="checkbox"/> Flow cytometry
<input checked="" type="checkbox"/>	<input type="checkbox"/> MRI-based neuroimaging

Unique biological materials

Policy information about [availability of materials](#)

Obtaining unique materials All plasmids listed in Supplementary table 4 are readily available upon reasonable request.

Antibodies

Antibodies used

Antibodies against Xenopus XLF, XRCC4, and IgG were used in this study.

Validation

These antibodies were previously validated as described in Ref 38.

Animals and other organisms

Policy information about [studies involving animals](#); [ARRIVE guidelines](#) recommended for reporting animal research

Laboratory animals

Xenopus laevis females older than 2 years were obtained from Nasco for use in this study.

Wild animals

Provide details on animals observed in or captured in the field; report species, sex and age where possible. Describe how animals were caught and transported and what happened to captive animals after the study (if killed, explain why and describe method; if released, say where and when) OR state that the study did not involve wild animals.

Field-collected samples

For laboratory work with field-collected samples, describe all relevant parameters such as housing, maintenance, temperature, photoperiod and end-of-experiment protocol OR state that the study did not involve samples collected from the field.